Supplementary Information. Homogeneous accretion of the Earth in the inner solar system

Paolo A. Sossi[1*] and Dan J. Bower[1]

[1*]Institute of Geochemistry and Petrology, Department of Earth and Planetary Sciences, ETH Zürich, Clausiusstrasse 25, Zürich, CH-8092, ZH, Switzerland.

*Corresponding author(s). E-mail(s): paolo.sossi@eaps.ethz.ch;
Contributing authors: dbower@eaps.ethz.ch;

Keywords: accretion, earth, isotope, inner solar system

1 Data Curation

1.1 Full Dataset

All data for the groups (error-weighted mean and standard error) used as a basis for producing the models and figures in this work can be found in the file '*NC_CC_AllData.csv*'. In the vast majority of cases, the group averages are identical to those reported in (1), which were calculated without outlier removal.

1.1.1 Molybdenum isotopic composition of the bulk silicate Earth

In determining the nucleosynthetic isotopic composition expressed in a given ratio, internal normalisation to a ratio of two, other isotopes is performed. For the isotopes of Mo, the normalisation is made by using the ^{98}Mo/^{96}Mo ratio, which is corrected to its assumed true value (1.453173, 2) from the value measured by mass spectrometry according to the exponential law (3). However, as first shown by (2), correcting the measured isotopic composition in this manner results in 'U-shaped' patterns when the $\varepsilon^{i/96}$Mo anomaly is expressed relative to the $^{i/96}$Mo ratio of a standard, plotted as a function of $^{i/96}$Mo (their Fig. 1). The authors concluded that $\varepsilon^{i/96}$Mo ratios calculated in this manner reflect the inadequate correction of the mass-dependent isotopic fractionation endemic to the sample. The conclusion is that this leads to spurious $\varepsilon^{i/96}$Mo ratios, should the mass-dependent isotopic fractionation diverge markedly from that of the standard.

In order to circumvent such artifacts, here we re-calculate the ε^{94}Mo and ε^{95}Mo composition of the bulk silicate Earth (BSE) using data that report both the mass-independent (i.e., nucleosynthetic) and mass-dependent compositions on the same, terrestrial sample. To do so, we use the data of (2) and (4). Mass-dependent isotopic compositions in the samples are expressed as δ^{98}Mo, where:

$$\delta^{98}Mo = \left[\frac{(^{98}Mo/^{95}Mo)_{smp}}{(^{98}Mo/^{95}Mo)_{std}} - 1\right] \times 1000. \quad \text{(S1)}$$

In Fig. S1, we find that ε^{94}Mo is strongly negatively correlated with δ^{98}Mo, whereas ε^{95}Mo is only weakly so given its closer proximity in atomic mass, to the normalising isotope ^{96}Mo. The linear fits were performed using the York regression scheme (see Methods, 5). As such, the accuracy of the ε^{94}Mo composition of the BSE, in particular, is sensitive to the appropriate selection of samples that have undergone minimal mass-dependent isotopic fractionation relative to the standard.

As shown in Fig. S1, the analysed samples in (2) and (4) define linear trends that overlap with one another, indicating no systematic offset between the two methods employed by the authors. Furthermore, such linearity is an indication that mass-dependent fractionation effects on the ε^{94}Mo ratio are not cumulative; that is, even if the δ^{98}Mo of a sample with a value close to that of the normalising standard was acquired through multiple mass fractionation events, this does not result in any substantial spurious ε^{94}Mo fractionation.

The key consideration in order to assess whether the BSE expresses nucleosynthetic Mo isotopic deviations from meteorites, is to ensure that the *relative* magnitude of

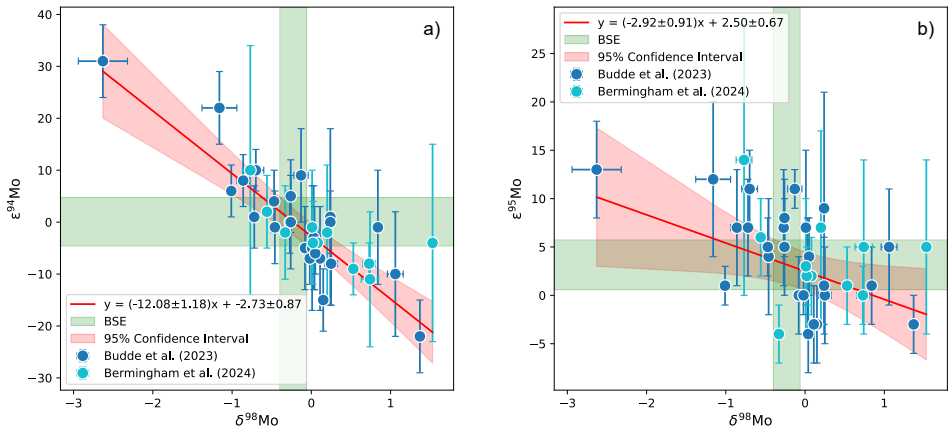

Fig. S1 Variations of the mass-dependent isotopic compositions of terrestrial samples, expressed as δ^{98}Mo, relative to those in nucleosynthetic isotopic anomalies corrected according to the exponential law and internally normalised to the ^{98}Mo/^{96}Mo ratio for a) ε^{94}Mo and b) ε^{95}Mo. All data are from (2) (blue points) and (4) (teal points). The red line represents the best fit to the data using the York regression (5) and the red field the 95 % confidence interval on the regression. The recovered of the bulk silicate Earth (BSE) for ε^{94}Mo and ε^{95}Mo for a range of δ^{98}Mo = -0.23±0.17, is given by the green, horizontal bar.

mass-dependent isotopic correction remains constant among them. That is, the samples chosen to represent the BSE value should have δ^{98}Mo isotopic values similar to those of meteorites to which it is compared. The range of δ^{98}Mo values among chondrites is close to -0.2 ‰ (e.g., 6), which is indistinguishable from that of the bulk silicate Earth (7; 8). Here, we take an average value of δ^{98}Mo = -0.23 ± 0.17 ‰, a conservative 2σ standard error to represent the range of plausible terrestrial and extraterrestrial compositions. This value is used in concert with the range of nucleosynthetic isotopic anomalies in Fig. S1 to derive values of ε^{94}Mo = 0.00 ± 0.05 and ε^{95}Mo = 0.03 ± 0.03, which are adopted throughout this study. These values lie between the previously reported estimates of 0.04 ± 0.06 and 0.10 ± 0.04 (9) and of -0.07 ± 0.03 and -0.01 ± 0.03 (4).

2 PCA / Bayesian Latent-Factor Analysis

2.1 Dataset for PCA / Bayesian Latent-Factor Analysis

The Principal Component Analysis (PCA) dimensionality reduction scheme is based on the principle that the principal components are computed by eigenvalue decomposition of the covariance matrix. The covariance matrix describes the correlation between any two values (here, isotope ratios) i and j, in a reservoir, R ($r \in 1, ..., R$), and is calculated as:

$$C_{ij} = \frac{1}{R}\sum_{r=1}^{R}(X_{r,i} - \hat{X}_i)(X_{r,j} - \hat{X}_j) \tag{S2}$$

where $X_{r,i}$ is the values of isotope ratio i in the r^{th} reservoir, and $\hat{X}_i$ is the mean of the i^{th} isotope ratio across all reservoirs. This leads to the condition that $X_{r,i}$ must exist across all i, otherwise the covariance matrix is undefined. To ensure sufficient data coverage, we apply a threshold, including only reservoirs with data for at least 8 out of the 10 isotope ratios, i (see the file '*NC_CC_AllData.csv*', Section 1.1) are selected for PCA / B-LFA. These are shown in Table S1.

Reservoir	Group	ε^{48}Ca	ε^{50}Ti	ε^{54}Cr	ε^{54}Fe	ε^{64}Ni	ε^{66}Zn	ε^{96}Zr	ε^{94}Mo	ε^{95}Mo	ε^{100}Ru
CI	CC	2.07 ± 0.07	1.91 ± 0.06	1.47 ± 0.09	0.031 ± 0.016	0.62 ± 0.10	0.30 ± 0.07	0.81 ± 0.16	0.79 ± 0.41	0.69 ± 0.25	-0.24 ± 0.13
CM	CC	3.13 ± 0.14	2.95 ± 0.10	0.98 ± 0.06	0.228 ± 0.027	0.37 ± 0.09	0.25 ± 0.05	1.23 ± 0.07	2.33 ± 0.90	1.42 ± 0.22	-0.69 ± 0.24
CO	CC	3.87 ± 0.56	3.41 ± 0.35	0.84 ± 0.13	0.163 ± 0.045	0.26 ± 0.11	0.24 ± 0.02	1.09 ± 0.07	1.31 ± 0.25	0.75 ± 0.17	-0.92 ± 0.45
CV	CC	2.51 ± 0.02	3.35 ± 0.14	0.91 ± 0.03	0.269 ± 0.036	0.30 ± 0.03	0.29 ± 0.04	1.16 ± 0.16	1.11 ± 0.04	1.01 ± 0.03	-1.06 ± 0.08
CR	CC	2.10 ± 0.02	2.22 ± 0.24	1.29 ± 0.06	0.323 ± 0.046	0.26 ± 0.15	0.30 ± 0.03	1.18 ± 0.09	2.22 ± 0.27	1.32 ± 0.19	-0.95 ± 0.13
H	NC	-0.24 ± 0.29	-0.57 ± 0.09	-0.38 ± 0.02	0.116 ± 0.047	-0.16 ± 0.05	-0.30 ± 0.05	0.34 ± 0.02	0.67 ± 0.07	0.29 ± 0.04	-0.30 ± 0.05
L	NC	-0.21 ± 0.05	-0.63 ± 0.02	-0.32 ± 0.06	0.106 ± 0.05	-0.11 ± 0.06	-0.25 ± 0.03	0.30 ± 0.03	0.59 ± 0.19	0.21 ± 0.11	-0.28 ± 0.13
LL	NC	-0.36 ± 0.02	-0.65 ± 0.05	-0.42 ± 0.05	0.129 ± 0.04	-0.18 ± 0.05	-0.27 ± 0.03	0.29 ± 0.02	0.62 ± 0.11	0.20 ± 0.06	*-0.29 ± 0.09**
EH	NC	-0.11 ± 0.02	-0.12 ± 0.07	0.00 ± 0.07	*0.064 ± 0.03**	0.07 ± 0.03	-0.16 ± 0.03	0.15 ± 0.05	0.45 ± 0.08	0.21 ± 0.06	-0.08 ± 0.08
EL	NC	-0.18 ± 0.04	-0.31 ± 0.06	0.03 ± 0.07	0.064 ± 0.03	-0.05 ± 0.04	-0.16 ± 0.04	0.17 ± 0.03	0.27 ± 0.04	0.12 ± 0.04	-0.08 ± 0.05
Ureilites	NC	-1.33 ± 0.05	-1.97 ± 0.15	-0.88 ± 0.04	0.149 ± 0.012	-0.20 ± 0.21	-0.34 ± 0.02	*0.50 ± 0.10**	0.93 ± 0.04	0.42 ± 0.03	-0.30 ± 0.05
Mars	NC	-0.20 ± 0.02	-0.44 ± 0.04	-0.18 ± 0.03	0.061 ± 0.02	0.08 ± 0.11	-0.20 ± 0.03	0.27 ± 0.02	0.33 ± 0.06	0.25 ± 0.04	*-0.17 ± 0.10**
Vesta Group†	NC	-0.99 ± 0.04	-1.30 ± 0.05	-0.69 ± 0.02	0.120 ± 0.025	*-0.19 ± 0.06**	*-0.30 ± 0.10**	0.38 ± 0.03	1.03 ± 0.03	0.47 ± 0.02	-0.42 ± 0.02
Earth	BSE	0.01 ± 0.04	0.01 ± 0.05	0.10 ± 0.12	-0.008 ± 0.019	0.12 ± 0.02	-0.07 ± 0.03	0.02 ± 0.02	0.00 ± 0.05	0.03 ± 0.03	0.02 ± 0.02

†Vesta Group is calculated as a weighted average of the following reservoirs: Vesta, Brachinites, Main Group Pallasites, Mesosiderites, Lodranites, Acapulcoites and Angrites. See text for more information.

*Indicates values that were estimated (not measured) in order to perform the PCA. See text for more information.

Table S1 Data for all reservoirs used in the PCA / B-LFA analysis.

Of the 14 reservoirs listed in Table S1, only the Vesta Group represents a composite reservoir, constructed from a weighted average of data for Vesta, Brachinites, Main Group Pallasites, Mesosiderites, Lodranites, Acapulcoites and Angrites. They are not taken to represent a single parent body, but as a group of small telluric bodies whose nucleosynthetic isotope ratios are similar to one another (see 10).

One rationale for doing so lies in the overlapping (Brachinites), indistinguishable (Mesosiderites) and similar (Main Group Pallasites) Δ^{17}O isotopic compositions of these three groups with those of the Howardite-Eucrite-Diogenite clan of meteorites from 4-Vesta (11). Indeed, Mesosiderites are thought to derive from the same parent body (i.e., 4-Vesta, 12), while Brachinites also share petrological features to HEDs in their high FeO contents (13). Main Group Pallasites are clearly distinguished from HEDs in Δ^{17}O, but their nucleosynthetic isotopic compositions for which data exist among the two meteorite groups (ε^{50}Ti, ε^{54}Cr and ε^{96}Zr) their compositions overlap within uncertainty. Angrites, acapulcoites and lodranites have distinct Δ^{17}O values to those from the aforementioned groups, yet, they too have ε^{50}Ti and ε^{54}Cr that overlap with those of other small telluric bodies (10).

For the reservoirs with less than 10 isotope ratios available, proxy values were estimated based on the following logic:

- **LL.** Missing value: ε^{100}Ru. Average of H and L chondrite values.
- **EH.** Missing value: ε^{54}Fe. Assumed identical to EL.
- **Ureilites.** Missing value: ε^{96}Zr. Estimated on the basis of linear correlations between ε^{96}Zr and other isotope ratios among the NC group.
- **Mars.** Missing value: ε^{100}Ru. Assumed intermediate between OC and EC bodies, as per other isotopic systems.
- **Vesta Group.** Missing values: ε^{64}Ni and ε^{66}Zn. Estimated on the basis of linear correlations between ε^{64}Ni and ε^{66}Zn with other iron-peak element isotopic ratios among NC bodies.

Finally, it should be noted that the PCA values are used only as *priors* for the B-LFA. The B-LFA yields the *posterior* probability function for each value, which differs from the prior value defined in Table S1.

2.2 Supplementary Results for PCA / Bayesian-Latent Factor Analysis

Raw output data for the PCA / B-LFA can be found in the Supplementary Files as '*elementset_idata_summary.xlsx*' where '*elementset*' corresponds to the set of isotope ratios used for the analysis (e.g., iron-peak). A summary of the variance explained by each of the principal components (PCs) in the PCA is given in Table S2.

An additional set of isotopic ratios, those corresponding to the lithophile elements, run in a manner identical to that used to produce Fig. 1 in the main text, is shown in Fig. S2, below.

The Isotopic Euclidean Distance, computed as the Euclidean Distance between an NC body, A and the BSE (d_{A-BSE}), referenced to that between the mean of the ordinary chondrites and the BSE (d_{OC-BSE}) in LF1-LF2 space, is denoted R_A. The

Table S2 Explained Variance (%) in Principal Component Analysis among different isotopic anomaly subsets.

	All	Siderophile	Iron-Peak	Heavy Element	Lithophile
PC1	73.59	71.20	78.68	86.00	90.54
PC2	16.53	18.85	16.02	9.76	6.06
PC3	5.03	7.13	3.46	3.31	2.52
PC4	2.32	2.52	1.21	0.93	0.63
PC1+PC2	90.12	90.05	94.70	95.76	96.60

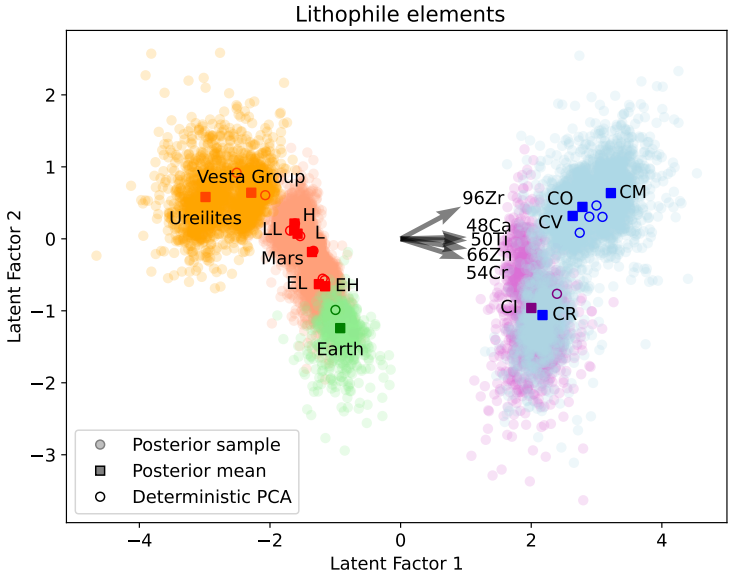

Fig. S2 Results of the Bayesian latent factor analysis (B-LFA) and deterministic Principal Component Analysis (PCA) across the nucleosynthetic isotopic compositions among the lithophile elements. See Table S1 for data. Refer to caption for Fig. 1 for more detail.

mean values of R_A and their uncertainties are given in Table S3 for different subsets of isotopic anomalies.

Table S3 Isotopic Euclidean Distances (R_A) among different isotopic anomaly subsets.

R_A	All	Siderophile	Iron-Peak	Heavy Element	Lithophile
BSE	0	0	0	0	0
EC	0.41±0.10	0.46±0.15	0.34±0.24	0.52±0.38	0.43±0.38
Mars	0.69±0.07	0.48±0.20	0.57±0.15	0.70±0.33	0.74±0.24
OC	1	1	1	1	1
Vesta Group	1.55±0.07	1.32±0.12	1.29±0.12	1.66±0.33	1.49±0.27

3 Multivariate Linear Regression

3.1 Dataset for Multivariate Linear Regression

The object of this exercise is to determine whether the bulk silicate Earth lies on an extension of the linear trend defined by the EH, EL, Mars, LL, L and H meteorites ('OC-EC' subgroup of the NC group) in Fig. 1 in the main text. It was shown in Fig. 1 that the Vesta Group and Ureilites fall off the linear array defined by these bodies in LF1-LF2 space, and are hence not included in the Multivariate Linear Regression (MLR).

Other meteorite groups are not included in Fig. 1 due to lack of available data across a sufficient number of isotopic systems (compare the data in the file '*NC_CC_AllData.csv*' with those in Table S1). In order to ascertain whether these bodies, which pertain largely to the iron meteorites and a selection of chondrite- (Kakangari, Rumuruti) and primitive achondrites (Aubrites, Winonaites), adhere to the trend defined by the OC-EC group in Fig. 1, we perform the same exercise (PCA / B-LFA) and examine their distribution in LF1-LF2 space. To do so, a more limited number of isotopic anomalies are implemented, namely,

- Subset 1 - Fig. S3a. ε^{54}Fe, ε^{64}Ni, ε^{94}Mo, ε^{95}Mo, ε^{100}Ru.
- Subset 2 - Fig. S3b. ε^{54}Cr, ε^{94}Mo, ε^{95}Mo, ε^{100}Ru.

The analysis shows that both the iron meteorite parent bodies and chondrite- and primitive achondrites are consistent with the linear trend defined by the OC-EC group. The Winonaites share affinities with the IAB iron meteorites in their Mo- and Ru isotopic compositions, consistent with their common origin inferred from O isotopes and petrologic considerations (14). Iron meteorites with more extreme nucleosynthetic isotope compositions (IIABs, IIIABs) also fall on an extension of the array defined by the 'OC-EC' subgroup. Consequently, these groups are included in the 'OC-EC' subgroup used to predict the composition of the BSE in the multivariate linear regressions, and the full dataset used in shown in Table S4.

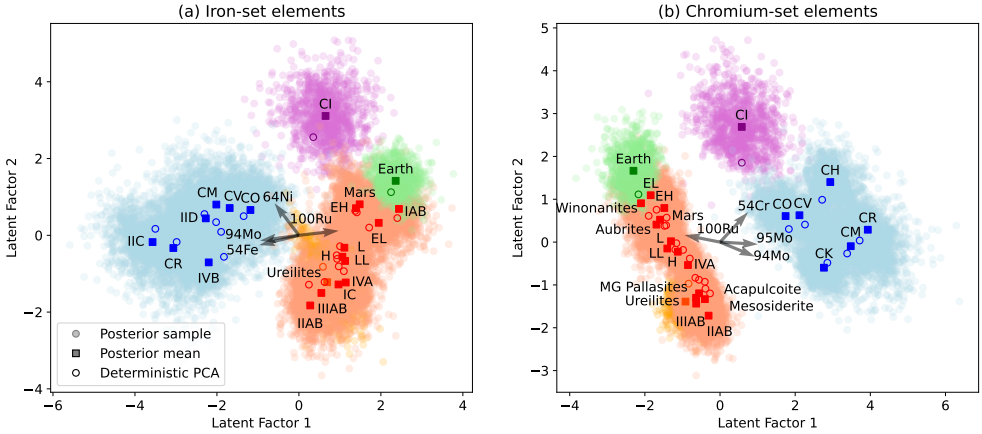

Fig. S3 Results of the Bayesian latent factor analysis (B-LFA) and deterministic Principal Component Analysis (PCA) across (a) Subset 1 and (b) Subset 2 with data taken for all available, individual reservoirs from the '*NC_CC_AllData.csv*' file. The iron meteorites (IAB, IVA, IC, IIAB, IIIAB) and the primitive achondrites (Aubrites, Winonaites) have LF1-LF2 characteristics consistent with those of the group consisting of H, L, LL, Mars, EH and EL (the 'OC-EC' subgroup; red). As per other groups of isotopic anomalies, the bulk silicate Earth (green) is an extension of the 'OC-EC' subgroup for all element groups, regardless of their chemical or nucleosynthetic affinity. Open circles are computed from deterministic PCA. Transparent, coloured circles show samples from the posterior distribution and filled squares are the means of the B-LFA. The arrows denote the loading vector for each isotopic ratio to the latent factors (e.g., a reservoir with high ε^{100}Ru will plot to lower values of LF1 at near-constant LF2 in panel (b)). The Bayesian analysis captures the uncertainty associated with the latent variables and the standard error on the observed data.

Reservoir	Group	Δ^{17}O	ε^{48}Ca	ε^{50}Ti	ε^{54}Cr	ε^{54}Fe	ε^{64}Ni	ε^{66}Zn	ε^{96}Zr	ε^{94}Mo	ε^{95}Mo	ε^{100}Ru
H	OC-EC	0.72 ± 0.05	-0.24 ± 0.29	-0.57 ± 0.09	-0.38 ± 0.02	0.116 ± 0.047	-0.16 ± 0.05	-0.30 ± 0.05	0.34 ± 0.02	0.67 ± 0.07	0.29 ± 0.04	-0.30 ± 0.05
L	OC-EC	1.03 ± 0.04	-0.21 ± 0.05	-0.63 ± 0.02	-0.32 ± 0.06	0.106 ± 0.05	-0.11 ± 0.06	-0.25 ± 0.03	0.30 ± 0.03	0.59 ± 0.19	0.21 ± 0.11	-0.28 ± 0.13
LL	OC-EC	1.19 ± 0.06	-0.36 ± 0.02	-0.65 ± 0.05	-0.42 ± 0.05	0.129 ± 0.04	-0.18 ± 0.05	-0.27 ± 0.03	0.29 ± 0.02	0.62 ± 0.11	0.20 ± 0.06	–
EH/Aub	OC-EC	0.00 ± 0.08	-0.11 ± 0.02	-0.10 ± 0.08	-0.02 ± 0.07	–	0.07 ± 0.03	-0.16 ± 0.03	0.19 ± 0.04	0.45 ± 0.08	0.22 ± 0.04	-0.06 ± 0.03
EL	OC-EC	-0.01 ± 0.07	-0.18 ± 0.04	-0.31 ± 0.06	0.03 ± 0.07	0.064 ± 0.03	-0.05 ± 0.04	-0.16 ± 0.04	0.17 ± 0.03	0.27 ± 0.04	0.12 ± 0.04	-0.08 ± 0.05
Kak	OC-EC	-1.09 ± 0.35	-1.30 ± 0.25	–	-0.44 ± 0.04	–	–	–	0.42 ± 0.04	–	–	–
Rum	OC-EC	2.64 ± 0.15	–	-0.47 ± 0.1	-0.06 ± 0.09	0.064 ± 0.03	–	–	0.25 ± 0.05	0.42 ± 0.09	0.18 ± 0.05	–
Win	OC-EC	-0.49 ± 0.07	-0.21 ± 0.09	-0.29 ± 0.11	-0.14 ± 0.04	–	–	–	0.02 ± 0.09	0.22 ± 0.06	0.09 ± 0.05	-0.06 ± 0.1
Mars	OC-EC	0.27 ± 0.03	-0.20 ± 0.02	-0.44 ± 0.04	-0.18 ± 0.03	0.061 ± 0.02	0.08 ± 0.11	-0.20 ± 0.03	0.27 ± 0.02	0.33 ± 0.06	0.25 ± 0.04	–
IAB	Iron Meteorites	–	–	–	–	-0.01 ± 0.02	-0.06 ± 0.06	-0.19 ± 0.13	–	0.04 ± 0.05	-0.04 ± 0.03	-0.02 ± 0.05
IC	Iron Meteorites	–	–	–	–	0.10 ± 0.05	-0.24 ± 0.09	-0.33 ± 0.05	–	0.88 ± 0.03	0.34 ± 0.01	-0.28 ± 0.03
IIAB	Iron Meteorites	-0.66 ± 0.13	–	–	-0.83 ± 0.03	0.16 ± 0.03	-0.29 ± 0.1	–	–	1.18 ± 0.02	0.51 ± 0.02	-0.43 ± 0.02
IIE	Iron Meteorites	0.57 ± 0.05	–	–	-0.59 ± 0.13	–	–	–	–	0.68 ± 0.05	0.30 ± 0.03	–
IIIAB	Iron Meteorites	-0.20 ± 0.04	–	–	-0.81 ± 0.05	0.10 ± 0.05	-0.32 ± 0.07	–	–	1.02 ± 0.05	0.44 ± 0.03	-0.50 ± 0.10
IIICD	Iron Meteorites	–	–	–	–	–	–	–	–	0.11 ± 0.03	-0.02 ± 0.04	–
IIIE	Iron Meteorites	–	–	–	–	–	-0.26 ± 0.08	–	–	0.95 ± 0.06	0.43 ± 0.04	-0.51 ± 0.06
IVA	Iron Meteorites	1.17 ± 0.10	–	–	-0.47 ± 0.06	0.10 ± 0.04	-0.28 ± 0.04	–	–	0.79 ± 0.04	0.40 ± 0.03	-0.28 ± 0.07

Table S4 Data for all (NC) reservoirs used in the MLR analysis. Values are given with their 2σ uncertainties (±). Missing data is denoted as "–". NB. Δ^{17}O data were not used in the analysis, but are listed here for completeness.

3.2 Supplementary Results for Multivariate Linear Regression

3.2.1 Correlation coefficient and Goodness-of-Fit

The York regression procedure described in the *Methods* section is applied to all binary combinations of isotope ratios (110 in total) for the NC bodies given in Table S4 to quantify $a \pm \sigma_a$ and $b \pm \sigma_b$ between each isotope pair. The results can be accessed in full in the '*regression_results.csv*' file. The Pearson correlation coefficient matrix is shown in Fig. S4 and the Goodness-of-Fit (GOF) matrix in Fig. S5.

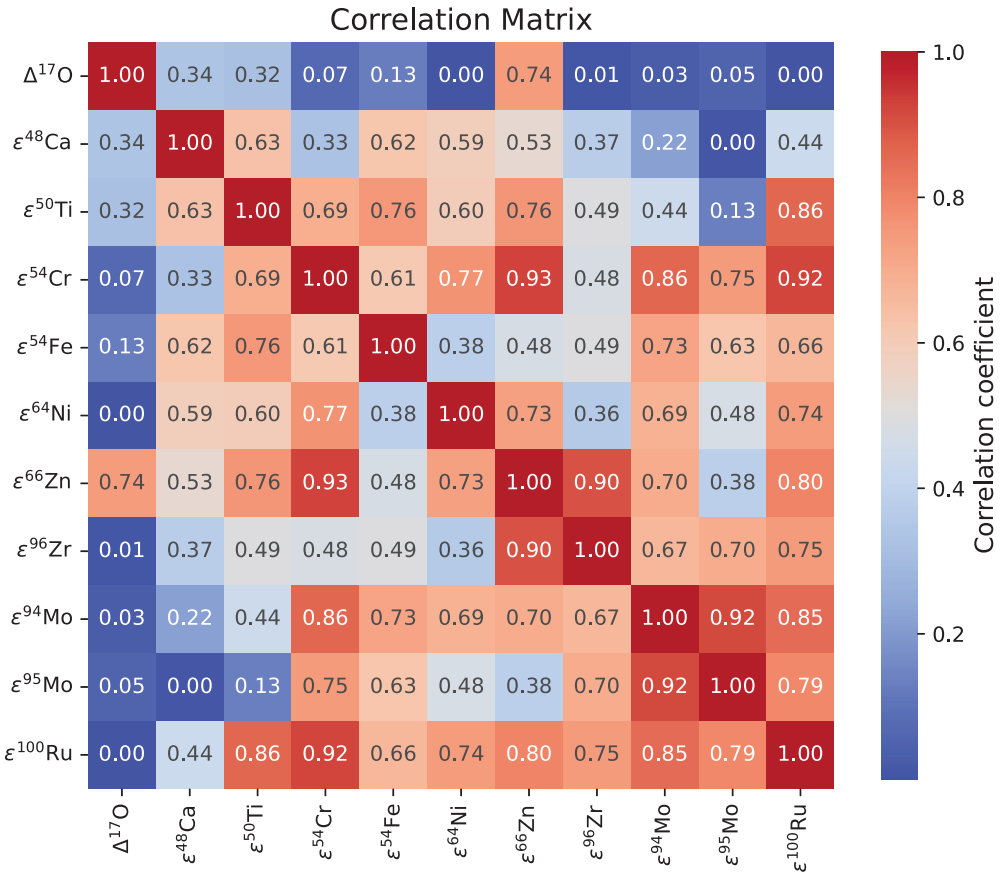

Fig. S4 Matrix showing the Pearson correlation coefficients (r^2) of binary isotope ratio pairs.

Immediately apparent is that the correlations between Δ^{17}O and the other isotopic systems in the NC meteorites is poor (<0.34, aside from 0.74 between ε^{66}Zn), a property reflected in the high (i.e., poor) Goodness-of-Fit (GOF). This observation substantiates the assertion that variations in Δ^{17}O are decoupled from those of the other isotopic systems. Variations in, for example, ε^{i}Mo ratios among meteorites

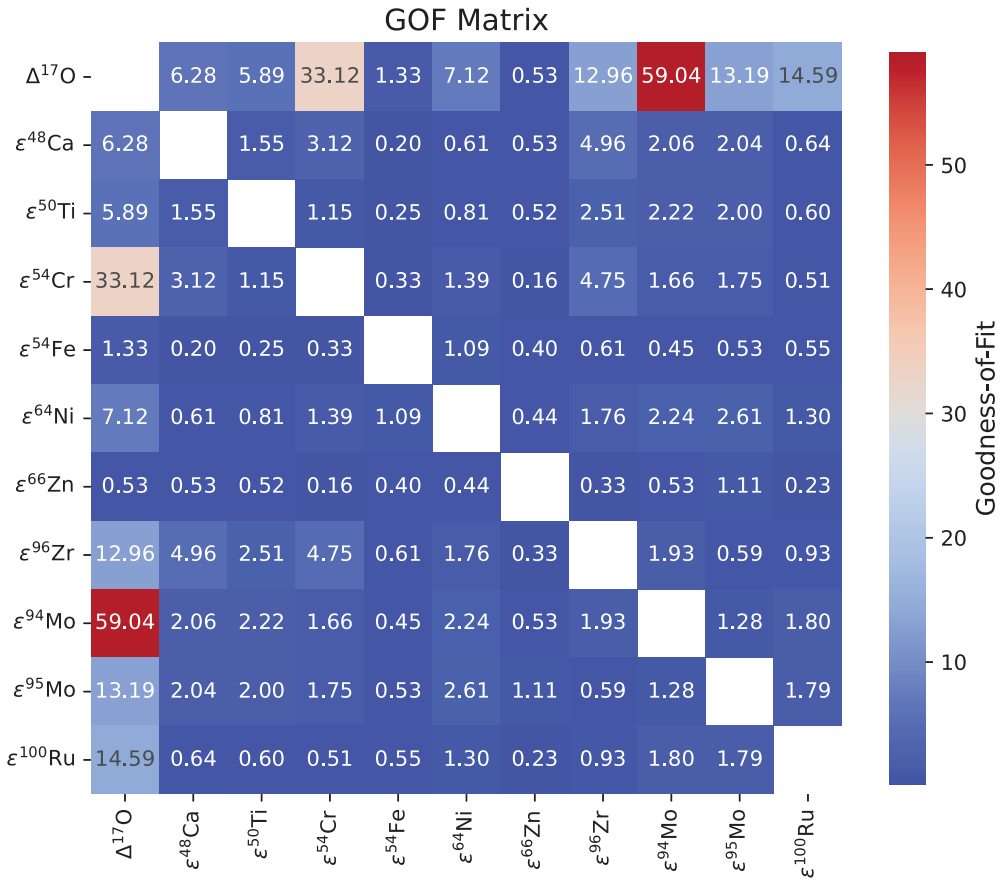

Fig. S5 Matrix showing the Goodness-of-Fit (eq. 13 of main text) of binary isotope ratio pairs.

can be modelled to result from different proportions of isotopes produced by the nucleosynthetic $r-$ and $s-$processes (e.g., 9; 15) or in ^{54}Cr by supernovae (16; 17). That there is no correlation in the variations of isotopes of both iron-peak and heavy elements with those of Δ^{17}O implies that the variations in the latter are not solely nucleosynthetic in origin (18). Consequently, they are excluded from the MLR analysis.

The correlations in the remaining 10 isotopic systems are strong among NC group meteorites. The mean correlation coefficient (r^2) across all isotope ratio is 0.61±0.21 (1 sd), with ε^{48}Ca being the only system for which the mean r^2 is below 0.5 (0.42±0.21, 1 sd), owing to the lack of high-precision data for certain meteorite groups (Kakangari and H chondrites, see Table S4). On the other hand, correlations between ε^{100}Ru and the other isotopic systems are uniformly high with the exception of with ε^{48}Ca, leading to an average r^2 of 0.76±0.14 (1 sd).

Goodness-of-Fit values with the exception of ε^{48}Ca vs. ε^{96}Zr, and ε^{96}Zr vs. ε^{54}Cr, are lower than 3. Should the linear regression between two quantities be a reasonable description of the data, then GOF values should be close to unity. In some cases, notably for ε^{54}Fe and ε^{66}Zn, the GOF is often below 1 (down to 0.16 for ε^{66}Zn vs. ε^{54}Cr), implying the residuals of the York fit to the data are better than expected given the uncertainties. This arises because the overall spread in isotopic ratios is low relative to the uncertainties for these two isotopic systems.

This exercise serve to underline that, in the vast majority of cases, variations between two isotopic systems are satisfactorily described by a linear regression. Therefore, isotopic variations among the group of NC meteorites shown in Table S4 are linearly correlated to a good approximation.

3.2.2 Prediction of the isotopic composition of the bulk silicate Earth

As described in the *Methods* section of the main text, the linear regression determined by York fit among the reservoirs in each binary ε-ε plot are used to compute the isotopic composition of the bulk silicate Earth (BSE), assuming *one* of the isotopic ratios is known (and is that of the BSE), termed the predictor, $x_{pred} \pm \sigma_{x_{pred}}$. To do so, a Monte Carlo simulation is run to sample the uncertainty in the predictor value, together with those in the slope and intercept of the regressions, 10,000 times assuming a Gaussian distribution about the mean values. This exercise yields a value for each of the remaining isotope systems, y^n_{BSE}, and the weighted mean across all predictor nine values are collated as $\hat{y}^n_{BSE}$. The weighted mean and associated standard error are shown in Table S5 and in the main text in Fig. 2.

Table S5 Predicted and observed isotopic composition of the bulk silicate Earth (BSE)

character	type	ratio	pred. mean ($\hat{y}_j$)	pred. st. err. ($\sigma_{\hat{y}_j}$)	obs. mean	obs. st. err.
lithophile	iron-peak	ε^{48}Ca	-0.03	0.02	0.01	0.04
lithophile	iron-peak	ε^{50}Ti	0.01	0.05	0.01	0.05
lithophile	iron-peak	ε^{54}Cr	0.17	0.03	0.10	0.12
siderophile	iron-peak	ε^{54}Fe	0.007	0.009	-0.008	0.019
siderophile	iron-peak	ε^{64}Ni	0.11	0.02	0.12	0.02
lithophile	iron-peak	ε^{66}Zn	-0.10	0.02	-0.07	0.03
lithophile	heavy	ε^{96}Zr	0.05	0.02	0.02	0.02
siderophile	heavy	ε^{94}Mo	0.05	0.03	0.00	0.05
siderophile	heavy	ε^{95}Mo	0.04	0.02	0.03	0.02
siderophile	heavy	ε^{100}Ru	0.03	0.02	0.02	0.02

In order to quantify the difference in the means of the distributions of the predicted values relative to the observed values of the BSE, the Z-score is computed for each predictor-predicted pair, according to:

$$Z = (y_{mod} - y_{obs})/\sqrt{\sigma^2_{mod} + \sigma^2_{obs}} \quad \text{(S3)}$$

where a Z-score < 1 indicates that the differences in the means of the two distributions are within one combined standard deviation of one another. The corresponding Z-score matrix is shown in Table S6 and in Fig. S6.

Table S6 Z-scores for binary isotope diagrams. Predictors are organised by columns and predicted values by rows.

	ε^{48}Ca	ε^{50}Ti	ε^{54}Cr	ε^{54}Fe	ε^{64}Ni	ε^{66}Zn	ε^{96}Zr	ε^{94}Mo	ε^{95}Mo	ε^{100}Ru
ε^{48}Ca		0.66	0.69	0.18	1.14	-0.31	-0.90	-0.46	2.24	0.94
ε^{50}Ti	-0.61		0.91	0.26	-0.17	-0.53	0.03	-0.10	-0.73	0.18
ε^{54}Cr	-0.64	-0.81		-1.25	-0.63	-0.65	0.32	-0.53	-0.85	-0.74
ε^{54}Fe	0.15	0.23	-1.78		0.85	0.11	-0.05	-0.51	-1.00	0.09
ε^{64}Ni	-0.93	0.14	0.63	0.86		-0.65	-1.06	0.15	0.50	0.86
ε^{66}Zn	0.50	0.92	1.08	0.17	1.29		-0.64	0.21	-0.09	0.66
ε^{96}Zr	-1.12	0.07	0.32	0.07	-1.85	-0.63		1.17	0.51	-0.97
ε^{94}Mo	-0.53	-0.13	-0.55	0.49	0.18	0.16	-1.35		-1.12	-0.32
ε^{95}Mo	-3.81	-1.35	-0.92	0.93	0.61	0.06	-0.41	1.12		0.27
ε^{100}Ru	-0.56	-0.17	0.80	0.10	-0.87	-0.40	-0.72	-0.31	0.26	

Converting the Z-scores into absolute differences, and comparing the averages for the different geochemical (i.e., lithophile or siderophile) and nucleosynthetic (i.e., iron-peak or heavy element) groups, no systematic difference in Z-scores is found (Table S7). The mean across all Z-scores is 0.65±0.55.

Table S7 Collated, absolute mean Z-scores between different isotopic groups according to their geochemical or nucleosynthetic affinity. Predictors are organised by columns and predicted values by rows.

	lithophile	siderophile
lithophile	0.73 ± 0.18	0.70 ± 0.26
siderophile	0.69 ± 0.38	0.57 ± 0.13
	iron-peak	heavy
iron-peak	0.68 ± 0.23	0.63 ± 0.23
heavy	0.75 ± 0.47	0.66 ± 0.21

Finally, visual representations of every binary ε-ε plot are shown, organised by predictor element, x_{pred}, in Figs. S7 to S16.

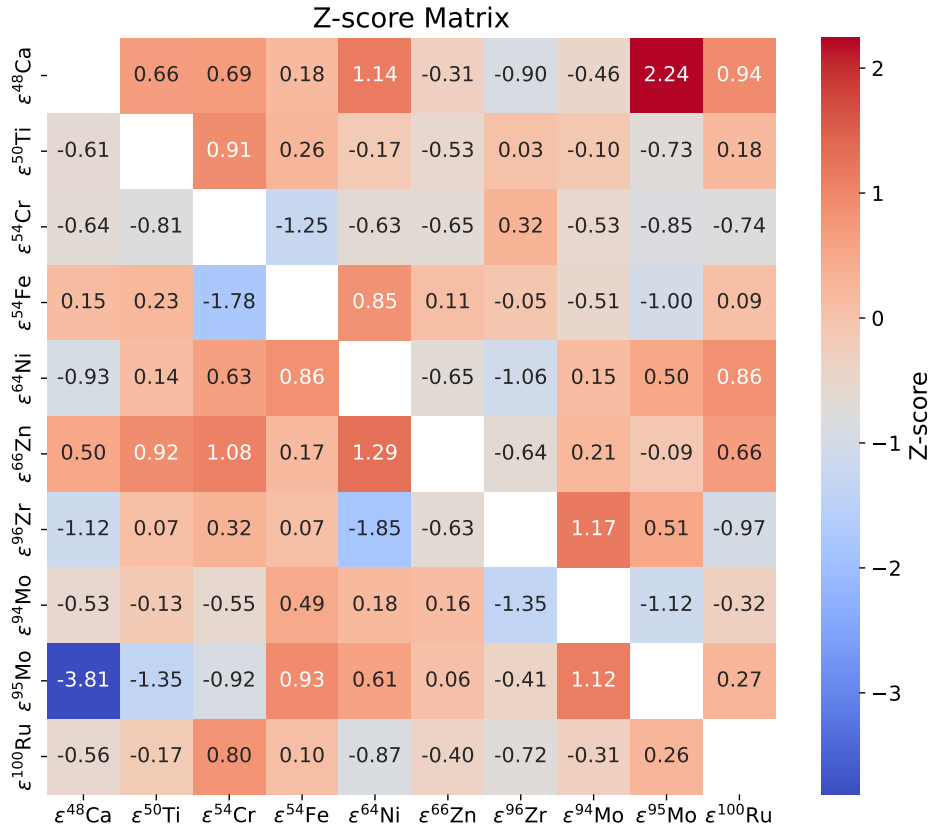

Fig. S6 Matrix showing the Z-score (eq. S3) of binary isotope ratios.

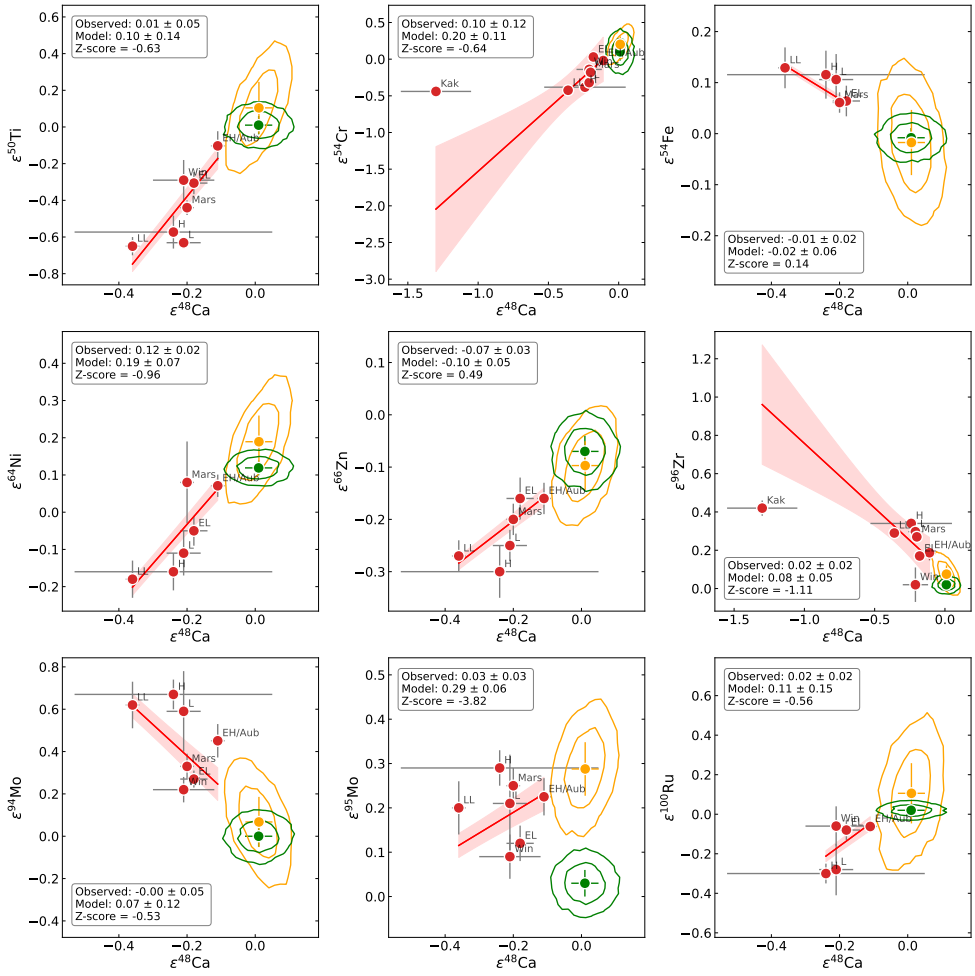

Fig. S7 Binary $\varepsilon^{i}x_{pred}$-$\varepsilon^{j}y$ plots in which the predictor is ε^{48}Ca. Data points denote analyses of reservoirs belonging to the OC-EC group (red points) and iron meteorites (grey points), with the York regression being shown as the red line with its 2-σ uncertainty envelope (red field). The observed- and predicted composition of the bulk silicate Earth (BSE) are given by the green- and yellow points and their 2-σ uncertainties, respectively. The green- and yellow fields delineate the regions within which 66 % and 95 % of the data lie for the observed- and predicted composition of the BSE, respectively. The caption also shows the Z-score value between the observed- and modelled BSE, computed as $Z\text{-score} = (y_{mod} - y_{obs})/\sqrt{\sigma^2_{mod} + \sigma^2_{obs}}$

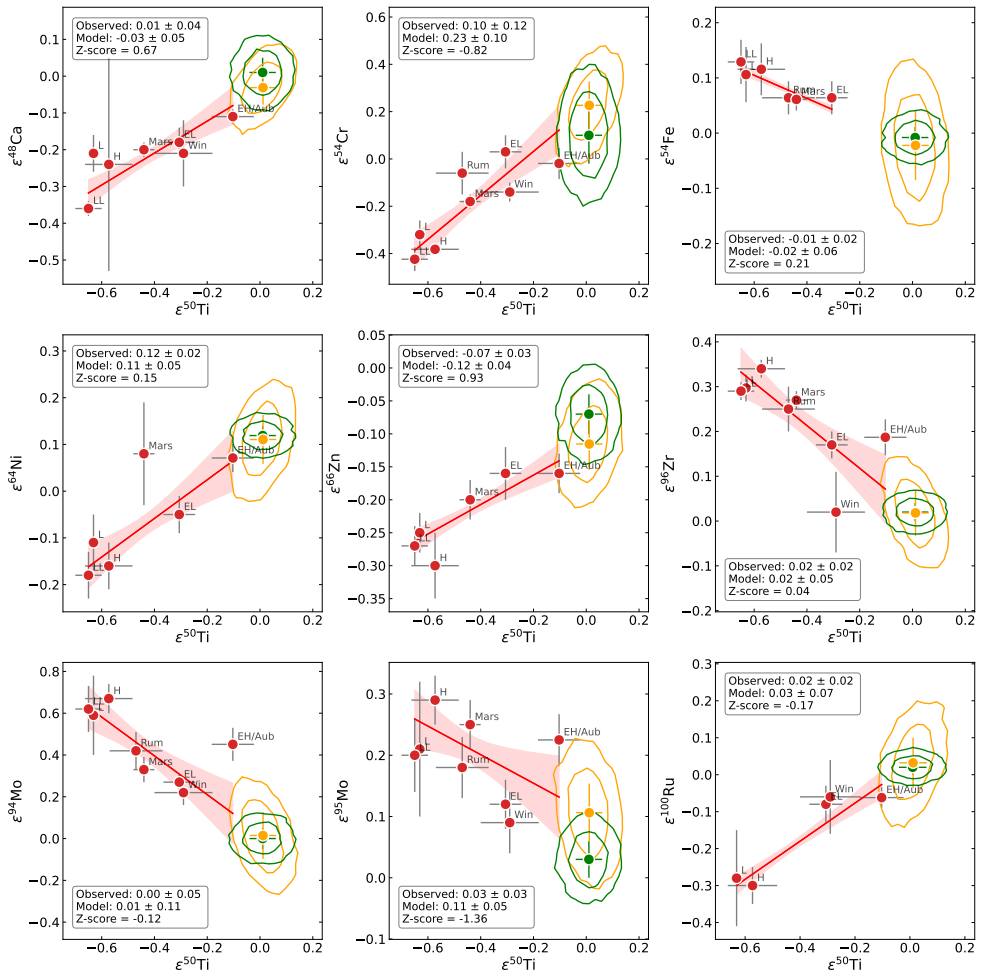

Fig. S8 Binary $\varepsilon^i x_{pred}$-$\varepsilon^j y$ plots in which the predictor is ε^{50}Ti. Data points denote analyses of reservoirs belonging to the OC-EC group (red points) and iron meteorites (grey points), with the York regression being shown as the red line with its 2-σ uncertainty envelope (red field). The observed- and predicted composition of the bulk silicate Earth (BSE) are given by the green- and yellow points and their 2-σ uncertainties, respectively. The green- and yellow fields delineate the regions within which 66 % and 95 % of the data lie for the observed- and predicted composition of the BSE, respectively. The caption also shows the Z-score value between the observed- and modelled BSE, computed as $Z\text{-score} = (y_{mod} - y_{obs})/\sqrt{\sigma^2_{mod} + \sigma^2_{obs}}$

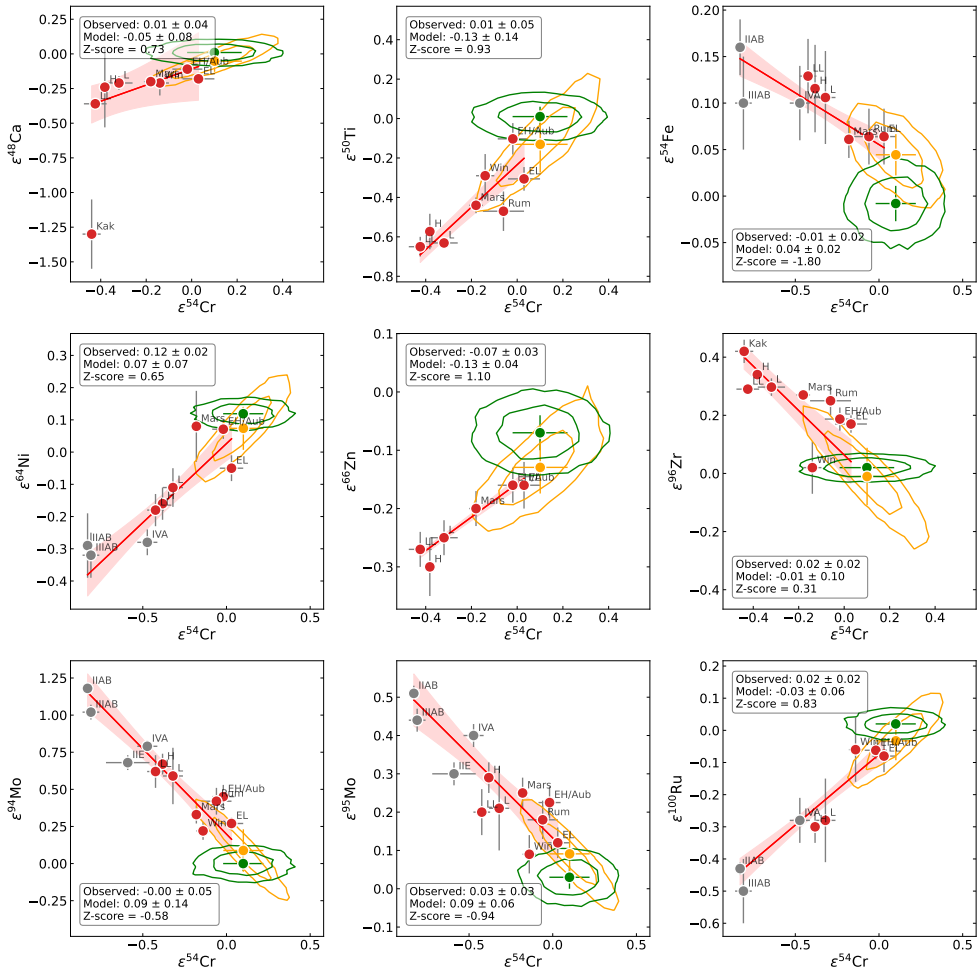

Fig. S9 Binary $\varepsilon^i x_{pred}$-$\varepsilon^j y$ plots in which the predictor is ε^{54}Cr. Data points denote analyses of reservoirs belonging to the OC-EC group (red points) and iron meteorites (grey points), with the York regression being shown as the red line with its 2-σ uncertainty envelope (red field). The observed- and predicted composition of the bulk silicate Earth (BSE) are given by the green- and yellow points and their 2-σ uncertainties, respectively. The green- and yellow fields delineate the regions within which 66 % and 95 % of the data lie for the observed- and predicted composition of the BSE, respectively. The caption also shows the Z-score value between the observed- and modelled BSE, computed as $Z\text{-score} = (y_{mod} - y_{obs})/\sqrt{\sigma^2_{mod} + \sigma^2_{obs}}$

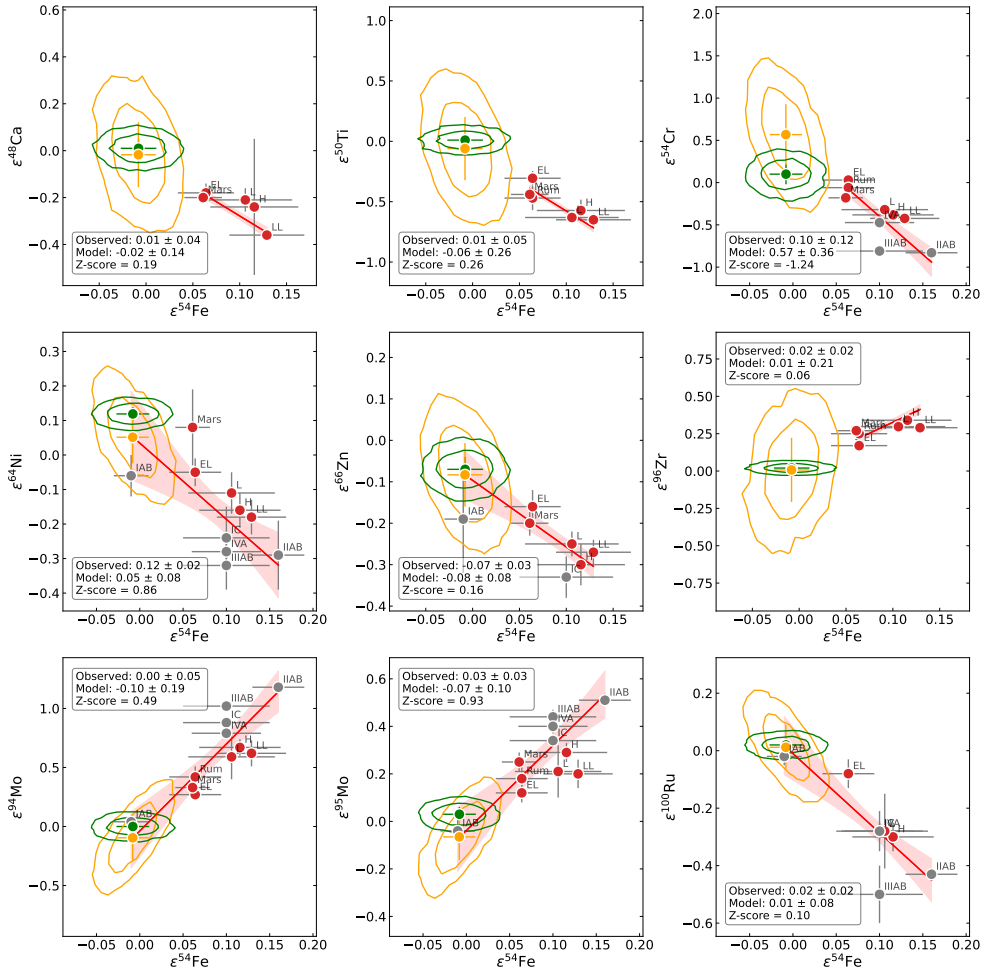

Fig. S10 Binary $\varepsilon^i x_{pred}$-$\varepsilon^j y$ plots in which the predictor is ε^{54}Fe. Data points denote analyses of reservoirs belonging to the OC-EC group (red points) and iron meteorites (grey points), with the York regression being shown as the red line with its 2-σ uncertainty envelope (red field). The observed- and predicted composition of the bulk silicate Earth (BSE) are given by the green- and yellow points and their 2-σ uncertainties, respectively. The green- and yellow fields delineate the regions within which 66 % and 95 % of the data lie for the observed- and predicted composition of the BSE, respectively. The caption also shows the Z-score value between the observed- and modelled BSE, computed as $Z\text{-score} = (y_{mod} - y_{obs})/\sqrt{\sigma^2_{mod} + \sigma^2_{obs}}$

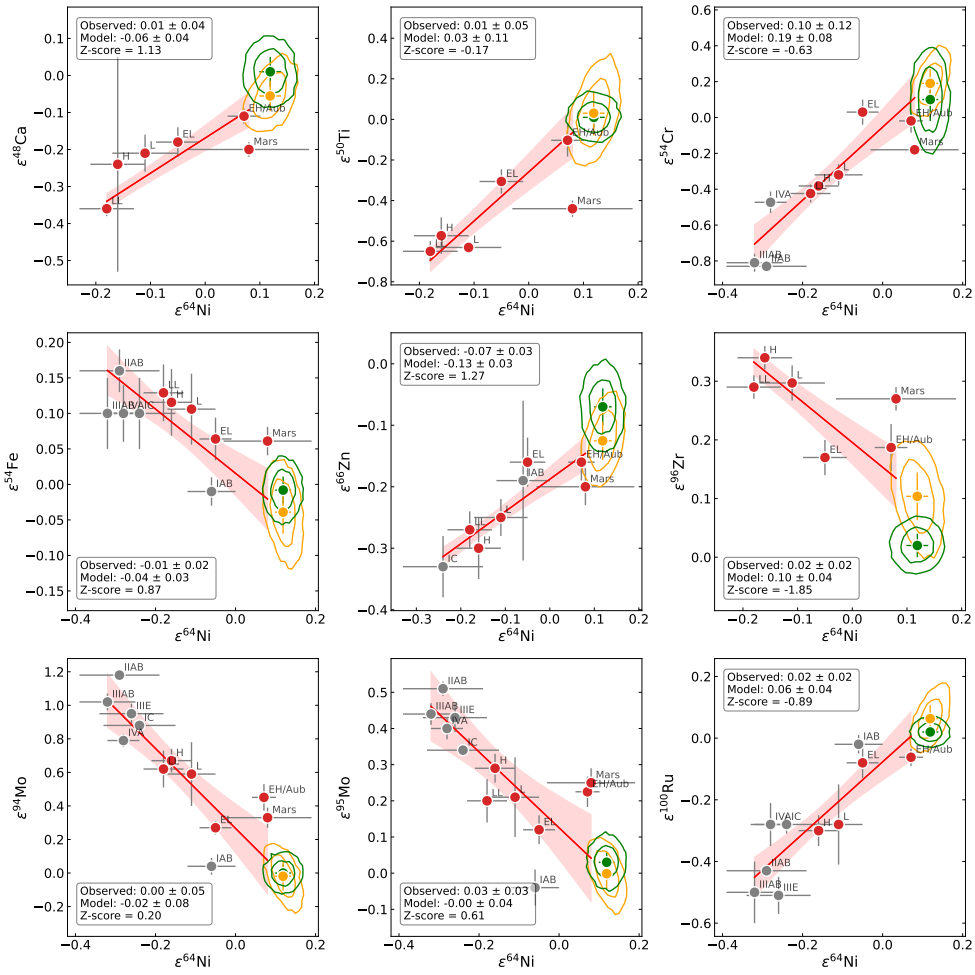

Fig. S11 Binary $\varepsilon^i x_{pred}$-$\varepsilon^j y$ plots in which the predictor is ε^{64}Ni. Data points denote analyses of reservoirs belonging to the OC-EC group (red points) and iron meteorites (grey points), with the York regression being shown as the red line with its 2-σ uncertainty envelope (red field). The observed- and predicted composition of the bulk silicate Earth (BSE) are given by the green- and yellow points and their 2-σ uncertainties, respectively. The green- and yellow fields delineate the regions within which 66 % and 95 % of the data lie for the observed- and predicted composition of the BSE, respectively. The caption also shows the Z-score value between the observed- and modelled BSE, computed as $Z\text{-score} = (y_{mod} - y_{obs})/\sqrt{\sigma^2_{mod} + \sigma^2_{obs}}$

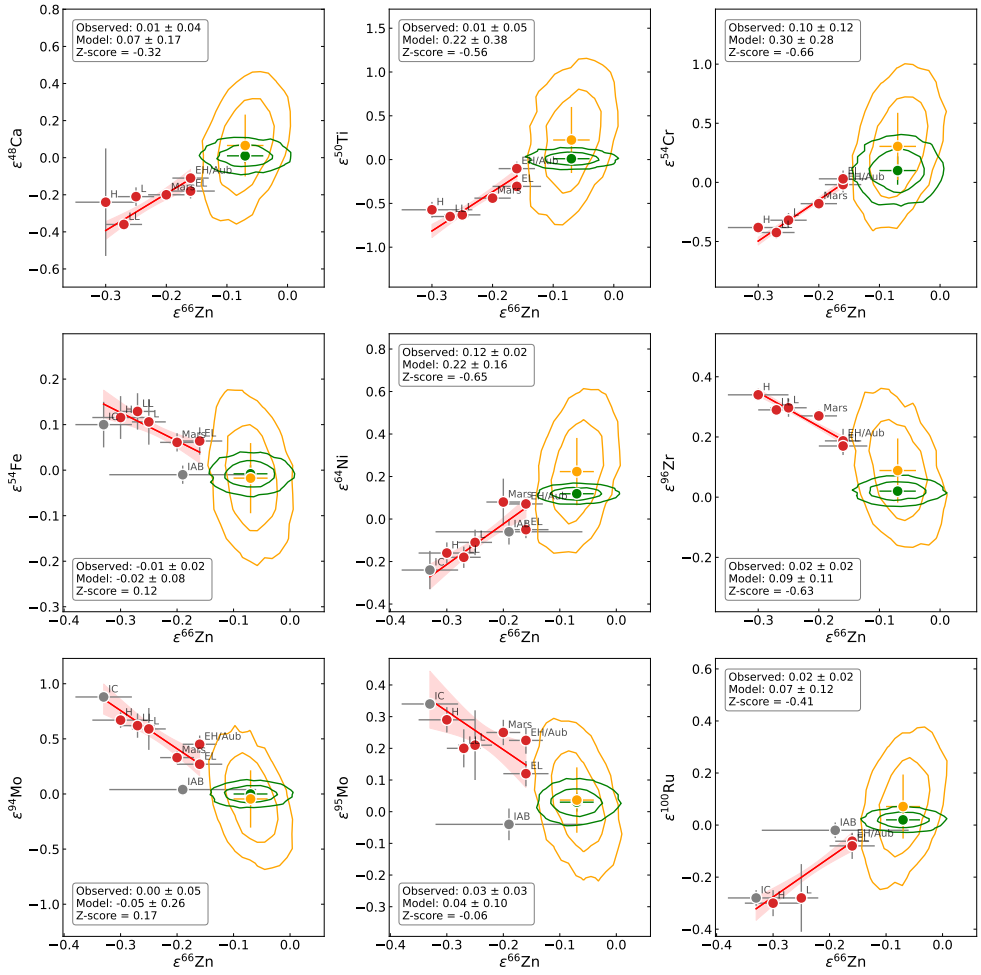

Fig. S12 Binary $\varepsilon^i x_{pred}$-$\varepsilon^j y$ plots in which the predictor is ε^{66}Zn. Data points denote analyses of reservoirs belonging to the OC-EC group (red points) and iron meteorites (grey points), with the York regression being shown as the red line with its 2-σ uncertainty envelope (red field). The observed- and predicted composition of the bulk silicate Earth (BSE) are given by the green- and yellow points and their 2-σ uncertainties, respectively. The green- and yellow fields delineate the regions within which 66 % and 95 % of the data lie for the observed- and predicted composition of the BSE, respectively. The caption also shows the Z-score value between the observed- and modelled BSE, computed as $Z\text{-score} = (y_{mod} - y_{obs})/\sqrt{\sigma^2_{mod} + \sigma^2_{obs}}$

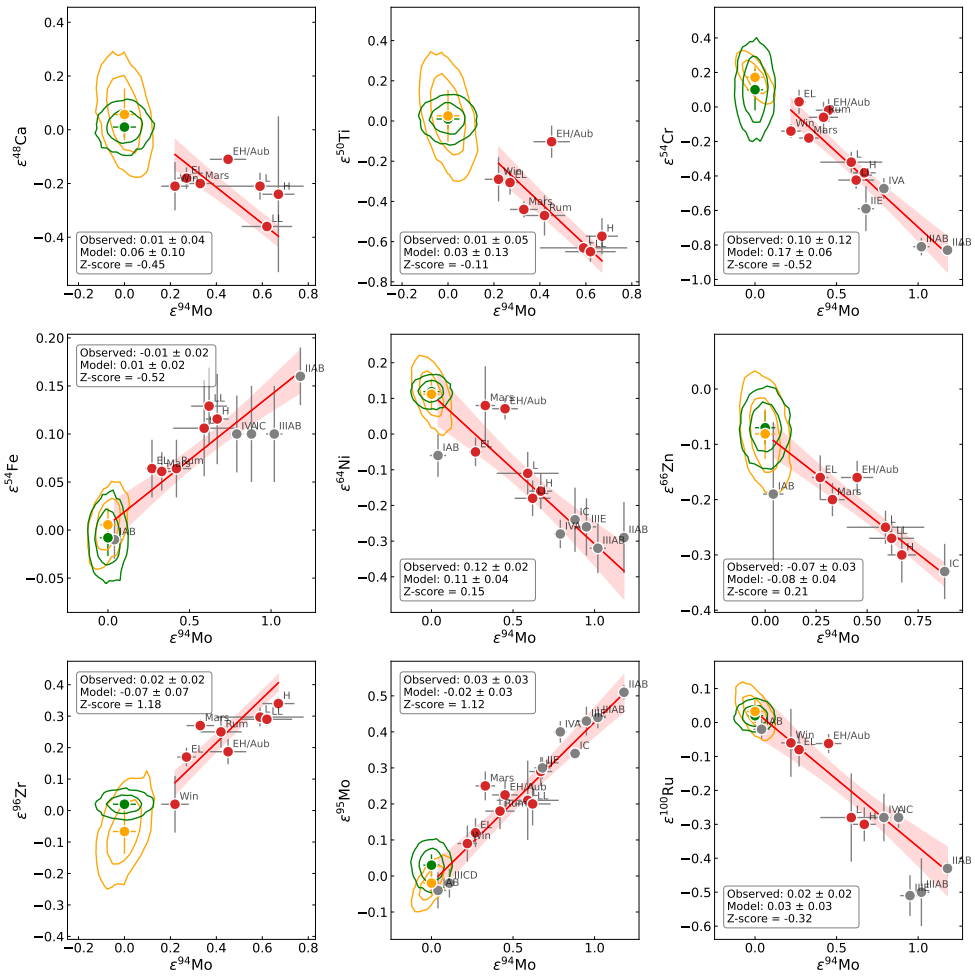

Fig. S13 Binary $\varepsilon^i x_{pred}$-$\varepsilon^j y$ plots in which the predictor is ε^{94}Mo. Data points denote analyses of reservoirs belonging to the OC-EC group (red points) and iron meteorites (grey points), with the York regression being shown as the red line with its 2-σ uncertainty envelope (red field). The observed- and predicted composition of the bulk silicate Earth (BSE) are given by the green- and yellow points and their 2-σ uncertainties, respectively. The green- and yellow fields delineate the regions within which 66 % and 95 % of the data lie for the observed- and predicted composition of the BSE, respectively. The caption also shows the Z-score value between the observed- and modelled BSE, computed as $Z\text{-score} = (y_{mod} - y_{obs})/\sqrt{\sigma^2_{mod} + \sigma^2_{obs}}$

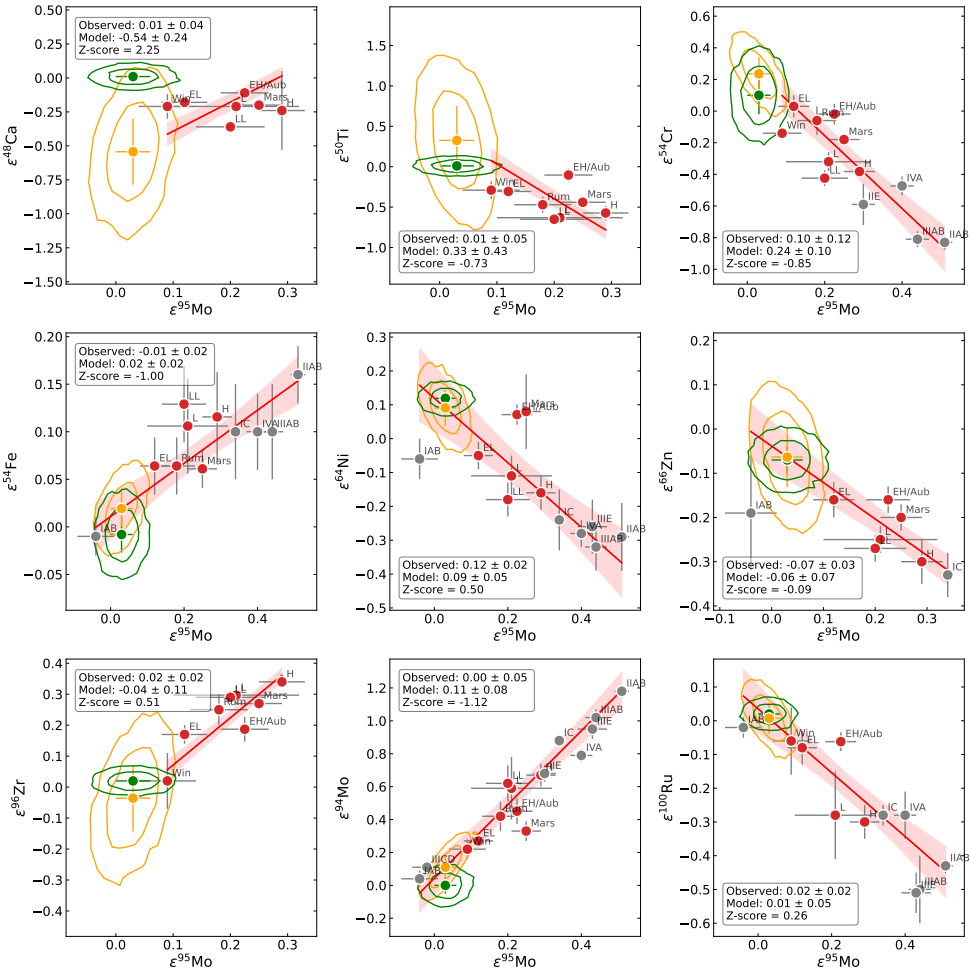

Fig. S14 Binary $\varepsilon^i x_{pred}$-$\varepsilon^j y$ plots in which the predictor is ε^{95}Mo. Data points denote analyses of reservoirs belonging to the OC-EC group (red points) and iron meteorites (grey points), with the York regression being shown as the red line with its 2-σ uncertainty envelope (red field). The observed- and predicted composition of the bulk silicate Earth (BSE) are given by the green- and yellow points and their 2-σ uncertainties, respectively. The green- and yellow fields delineate the regions within which 66 % and 95 % of the data lie for the observed- and predicted composition of the BSE, respectively. The caption also shows the Z-score value between the observed- and modelled BSE, computed as $Z\text{-score} = (y_{mod} - y_{obs})/\sqrt{\sigma^2_{mod} + \sigma^2_{obs}}$

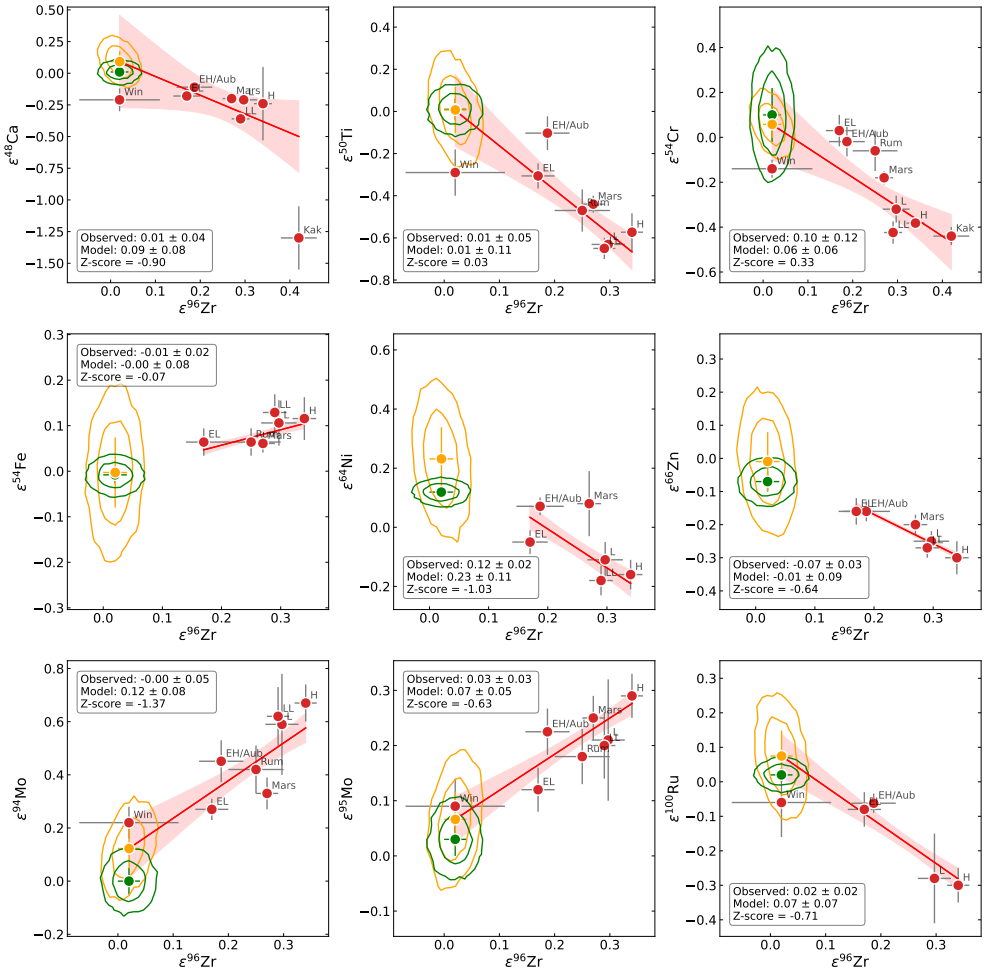

Fig. S15 Binary $\varepsilon^{i}x_{pred}$-$\varepsilon^{j}y$ plots in which the predictor is ε^{96}Zr. Data points denote analyses of reservoirs belonging to the OC-EC group (red points) and iron meteorites (grey points), with the York regression being shown as the red line with its 2-σ uncertainty envelope (red field). The observed- and predicted composition of the bulk silicate Earth (BSE) are given by the green- and yellow points and their 2-σ uncertainties, respectively. The green- and yellow fields delineate the regions within which 66 % and 95 % of the data lie for the observed- and predicted composition of the BSE, respectively. The caption also shows the Z-score value between the observed- and modelled BSE, computed as $Z\text{-score} = (y_{mod} - y_{obs})/\sqrt{\sigma^2_{mod} + \sigma^2_{obs}}$

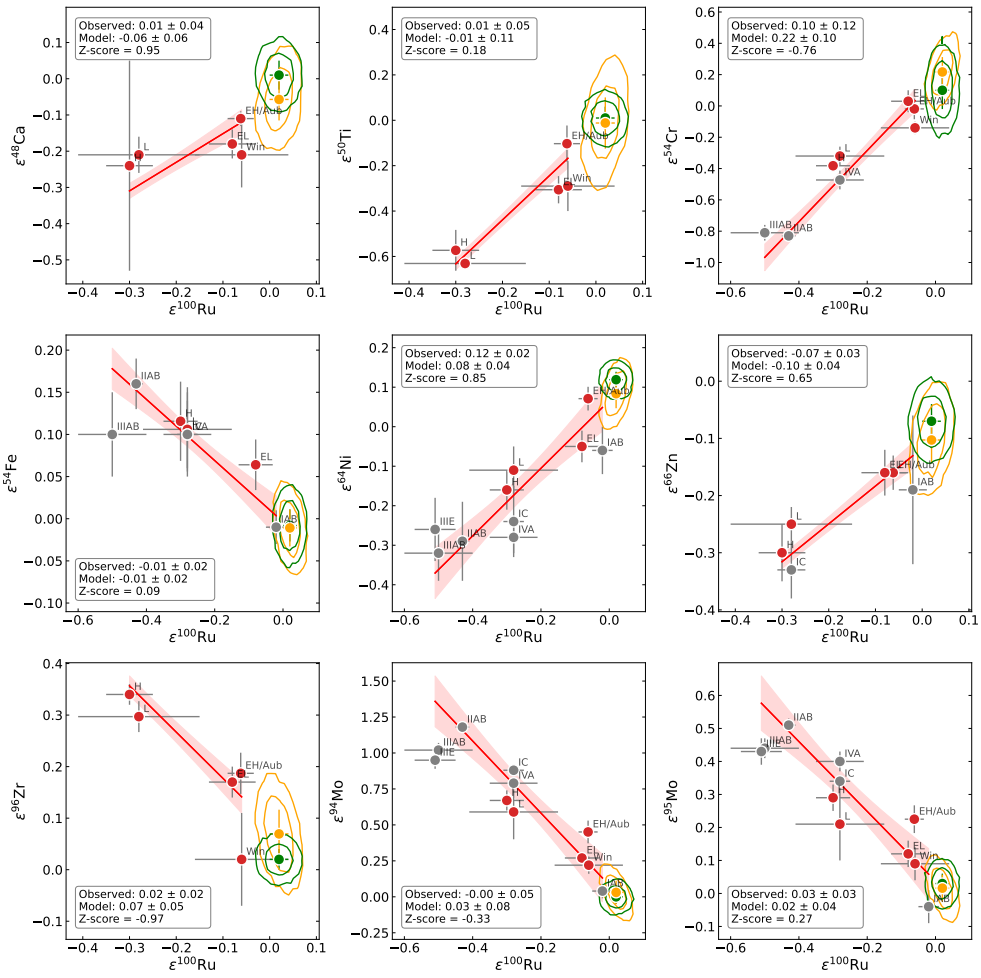

Fig. S16 Binary $\varepsilon^i x_{pred}$-$\varepsilon^j y$ plots in which the predictor is ε^{100}Ru. Data points denote analyses of reservoirs belonging to the OC-EC group (red points) and iron meteorites (grey points), with the York regression being shown as the red line with its 2-σ uncertainty envelope (red field). The observed- and predicted composition of the bulk silicate Earth (BSE) are given by the green- and yellow points and their 2-σ uncertainties, respectively. The green- and yellow fields delineate the regions within which 66 % and 95 % of the data lie for the observed- and predicted composition of the BSE, respectively. The caption also shows the Z-score value between the observed- and modelled BSE, computed as $Z\text{-score} = (y_{mod} - y_{obs})/\sqrt{\sigma^2_{mod} + \sigma^2_{obs}}$

4 Prediction of the isotopic compositions of Venus and Mercury

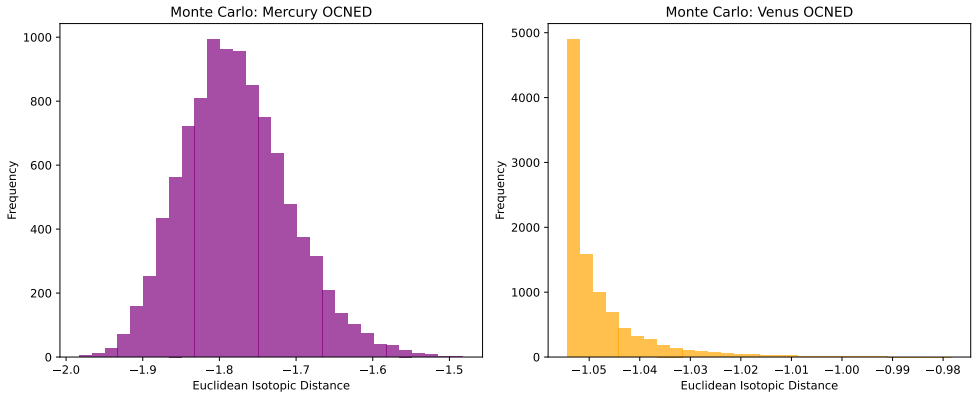

Fig. S17 Posterior distributions of the Isotopic Euclidean Distances (R_A) of Venus and Mercury as computed from 10^4 Monte Carlo simulations of fits of mass-conserving Gaussians to the R_A values of Earth, Mars and Vesta (Fig. 3), themselves calculated using all 10 isotopic anomalies (Fig. 1a).

References

[1] Dauphas, N., Hopp, T. & Nesvorný, D. Bayesian inference on the isotopic building blocks of Mars and Earth. *Icarus* **408**, 115805 (2024).

[2] Budde, G., Tissot, F. L., Kleine, T. & Marquez, R. T. Spurious molybdenum isotope anomalies resulting from non-exponential mass fractionation. *Geochemistry* **83**, 126007 (2023).

[3] Albarede, F. *et al.* Precise and accurate isotopic measurements using multiple-collector icpms. *Geochimica et Cosmochimica Acta* **68**, 2725–2744 (2004).

[4] Bermingham, K. R. *et al.* The non-carbonaceous nature of earth's late-stage accretion. *Geochimica et Cosmochimica Acta* (2024).

[5] York, D., Evensen, N. M., Martınez, M. L. & De Basabe Delgado, J. Unified equations for the slope, intercept, and standard errors of the best straight line. *American journal of physics* **72**, 367–375 (2004).

[6] Burkhardt, C., Hin, R. C., Kleine, T. & Bourdon, B. Evidence for mo isotope fractionation in the solar nebula and during planetary differentiation. *Earth and Planetary Science Letters* **391**, 201–211 (2014).

[7] McCoy-West, A. J. *et al.* Extensive crustal extraction in earth's early history inferred from molybdenum isotopes. *Nature Geoscience* **12**, 946–951 (2019).

[8] Hin, R. C. *et al.* The influence of crustal recycling on the molybdenum isotope composition of the earth's mantle. *Earth and Planetary Science Letters* **595**, 117760 (2022).

[9] Budde, G., Burkhardt, C. & Kleine, T. Molybdenum isotopic evidence for the late accretion of outer Solar System material to Earth. *Nature Astronomy* **3**, 736–741 (2019).

[10] Rüfenacht, M. *et al.* Genetic relationships of solar system bodies based on their nucleosynthetic Ti isotope compositions and sub-structures of the solar protoplanetary disk. *Geochimica et Cosmochimica Acta* **355**, 110–125 (2023).

[11] Greenwood, R., Franchi, I., Gibson, J. & Benedix, G. Oxygen isotope variation in primitive achondrites: The influence of primordial, asteroidal and terrestrial processes. *Geochimica et Cosmochimica Acta* **94**, 146–163 (2012).

[12] Haba, M. K., Wotzlaw, J.-F., Lai, Y.-J., Yamaguchi, A. & Schönbächler, M. Mesosiderite formation on asteroid 4 vesta by a hit-and-run collision. *Nature Geoscience* **12**, 510–515 (2019).

[13] Keil, K. Brachinite meteorites: Partial melt residues from an feo-rich asteroid. *Geochemistry* **74**, 311–329 (2014). SI: 100 years.

[14] Benedix, G., McCoy, T. J., Keil, K. & Love, S. A petrologic study of the iab iron meteorites: Constraints on the formation of the iab-winonaite parent body. *Meteoritics & Planetary Science* **35**, 1127–1141 (2000).

[15] Ek, M., Hunt, A. C., Lugaro, M. & Schönbächler, M. The origin of s-process isotope heterogeneity in the solar protoplanetary disk. *Nature Astronomy* **4**, 273–281 (2020).

[16] Woosley, S. E. & Heger, A. Nucleosynthesis and remnants in massive stars of solar metallicity. *Physics Reports* **442**, 269–283 (2007).

[17] Dauphas, N. *et al.* Neutron-rich chromium isotope anomalies in supernova nanoparticles. *The Astrophysical Journal* **720**, 1577 (2010).

[18] Lyons, J. & Young, E. Co self-shielding as the origin of oxygen isotope anomalies in the early solar nebula. *Nature* **435**, 317–320 (2005).

5 Acknowledgments

PAS and DJB were supported by the Swiss State Secretariat for Education, Research and Innovation (SERI) under contract No. MB22.00033, a SERI-funded ERC Starting grant "2ATMO". PAS also thanks the Swiss National Science Foundation (SNSF) through an Eccellenza Professorship (#203668).

6 Author contributions

PAS conceived the study, ran the PCA, developed the multivariate analysis and gaussian fitting model and wrote the paper. DJB developed the PCA and B-LFA analyses and contributed to writing the paper.

7 Additional information

All .csv and .xlsx files cited in the text can be found in '*Supplementary_Data.zip*'.